Asymmetric dual Bloch point domain walls in cylindrical magnetic nanowires

J. Askey, M. Hunt, W. Langbein, et al.

COLLECTIONS

Paper published as part of the special topic on Science and Technology of 3D Magnetic Nanostructures

View Online   Export Citation   CrossMark

ARTICLES YOU MAY BE INTERESTED IN

Bloch point dynamics in exchange-spring heterostructures
APL Materials 10, 071103 (2022); https://doi.org/10.1063/5.0097610

Chinese Abstracts
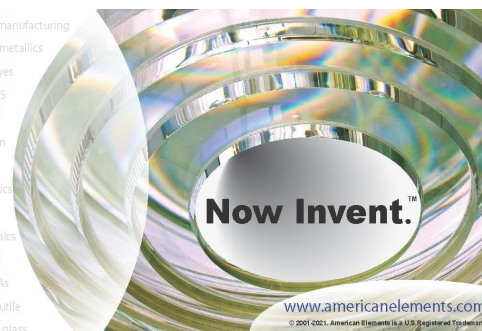Chinese Journal of Chemical Physics 35, i (2022); https://doi.org/10.1063/1674-0068/35/02/cabs

Modal-MUSIC: A passive mode estimation algorithm for partially spanning arrays
JASA Express Letters 2, 074802 (2022); https://doi.org/10.1121/10.0012041

Asymmetric dual Bloch point domain walls in cylindrical magnetic nanowires

View Online   Export Citation   CrossMark

J. Askey, [ID] M. Hunt, [ID] W. Langbein, [ID] and S. Ladak[a] [ID]

AFFILIATIONS

School of Physics and Astronomy, Cardiff University, Cardiff CF24 3AA, United Kingdom

Note: This paper is part of the Special Topic on Science and Technology of 3D Magnetic Nanostructures.
[a]Author to whom correspondence should be addressed: LadakS@cardiff.ac.uk

ABSTRACT

Cylindrical magnetic nanowires have been studied extensively over the past ten years due to the presence of domain walls with novel topology and outstanding dynamic properties. In soft magnetic systems, where shape anisotropy forces the magnetization along the wire axis, and for radii above 50 nm, two topologically distinct walls have been previously identified. The Bloch point wall (BPW) has a circulating magnetization texture around the circumference and contains a single Bloch point within the center of the wire cross section. In contrast, asymmetric transverse walls (ATWs) have a circulating magnetization structure on the surface and contain two topological defects, a vortex and an anti-vortex on opposing sides. These surface defects are connected via a vortex tube that penetrates the volume. In this study, we have numerically investigated the domain wall magnetization textures for nickel nanowires of radii 50–120 nm. Beyond reproducing the known BPW and ATW topology, we discover a new domain wall type that contains aspects of both. This new domain wall type, which we call asymmetric dual Bloch point wall (ADBPW), has surface vortices similar to an ATW and two Bloch-point textures adjacent to the internal vortex tube. Time-resolved simulations investigating the stability of ADBPW show its field-driven transformation into a BPW via the ejection of a single Bloch point at the surface and subsequent annihilation of surface vortices.

Three-dimensional (3D) magnetic nanostructures have recently emerged as a platform to explore interesting spin textures through intricate control of 3D geometry,[1–5] topology,[6–9] and frustration.[10,11] In particular, cylindrical magnetic nanowires (NWs) have proven to be a reliable system to demonstrate a diverse range of physics including the stabilization of spin textures with novel topology, such as Bloch points, helical domain walls,[12] and Skyrmion tubes,[13–15] as well as important dynamic phenomena such as the spin Cherenkov effect[16] and field-driven dynamic transformation of the domain wall topology.[5] Such systems also hold promise in a diverse range of technological applications, including data storage,[17,18] logic devices,[19] smart drug delivery,[20] and cancer treatment.[21]

From an experimental point of view, 3D NWs are attractive for a multitude of reasons. These systems are readily fabricated using cheap and relatively simple methodologies, the most prominent being that of the electrodeposition into anodized alumina templates.[22–24] This methodology allows one to access NWs with diameters in the range of 100 nm and below, with lengths in

the micron range, allowing aspect ratios above 20 to be achieved. Recently, the achievable complexity of the NWs using the above method has been extended into arrays of interconnected NWs.[25] In addition, more complex techniques such as two-photon lithography (TPL)[26–28] and focused electron beam deposition (FEBD)[29,30] can be used to place cylindrical magnetic nanowires into arbitrary geometries, allowing one to probe the impact of curvature and 3D defects.

The energetic phase diagram of single $Ni_{81}Fe_{19}$ (Permalloy) NWs has been reported by Ferguson et al.,[31] which illustrates the existence of three domain wall (DW) types in the radius range spanning 5–50 nm. These results have been further reported in the work by Jamet et al.,[32] simulating a radius range spanning 10–70 nm. At low radii, transverse walls (TWs) are observed as the lowest energy state, while at high radii, Bloch-point domain walls (BPWs) become favorable. This is a consequence of the increasing relative contribution of the magnetostatic energy with the radius, making it energetically favorable to avoid the strong stray fields of TWs by the curling of the magnetization circumferentially about the NW, at the

cost of higher exchange energy. The resulting BPW contains a Bloch point (BP) in its center as part of its topology. Notably, other DW types that have higher energies can be rendered metastable by an energy barrier in the transformation to the lowest energy DW. One example of such a metastable DW is observed in the BPW regime and is known as the asymmetric transverse wall (ATW, labeled as a transverse vortex wall by Jamet et al.[32]), with energy slightly above that of the BPW.[31] The ATW surface magnetization texture is shown in Fig. 1(a), exemplifying the surface vortex characteristic of this DW type. The accompanying isosurfaces for a component of the magnetization $M_z = \pm 0.8$ is shown in Fig. 1(b), which illustrates the vortex tube connecting the surface vortex (top) to the anti-vortex (bottom). Figures 1(c) and 1(d) show the corresponding surface textures and isosurfaces for the BPW. The surface texture illustrates the wrapping of local magnetization about the surface of the wire, and the volume isosurfaces illustrate the BP location where the radial magnetization component changes sharply and local magnetization vanishes.

In this article, we report on the study of soft magnetic cylindrical NWs of a fixed length and radius that varies between 50 and 120 nm in 10 nm steps, using finite-difference micromagnetic simulations. We observe the typical BPW and ATW relaxed states as reported previously[31] and, above a threshold radius, we further observe the existence of a new DW type showing topological characteristics of both the BPW and ATW.

The micromagnetic simulations were performed using MuMax3[33] and Ubermag,[34,35] both of which employ a finite-difference discretization of the simulation space in order to solve the Landau–Lifshitz–Gilbert (LLG) equation,

$$\frac{d\boldsymbol{M}}{dt} = -\gamma_0 (\boldsymbol{M} \times \boldsymbol{H}_{eff}) + \alpha \left(\boldsymbol{M} \times \frac{d\boldsymbol{M}}{dt} \right). \tag{1}$$

Here, $\boldsymbol{M}$ is the normalized magnetization vector, $\gamma_0 = 2.211 \times 10^5$ m A^{-1} s^{-1} is the gyromagnetic ratio, α is a phenomenological damping constant, and $\boldsymbol{H}_{eff}$ is the effective field,

$$\boldsymbol{H}_{eff} = \frac{-1}{\mu_0 M_s} \frac{\delta \varepsilon [\boldsymbol{M}]}{\delta \boldsymbol{M}}, \tag{2}$$

where ε is the energy density, $\frac{\delta \varepsilon [\boldsymbol{M}]}{\delta \boldsymbol{M}}$ is the variational derivative of the energy density with respect to the normalized magnetization, M_s is the saturation magnetization, and $\mu_0 = 1.2566 \times 10^{-6}$ H m^{-1}. Material parameters of nickel (Ni) were used[36] with the exchange stiffness, $A_{ex} = 9 \times 10^{-12}$ J m^{-1} and $M_s = 4.9 \times 10^5$ A m^{-1}. The exchange length is defined as

$$l_{ex} = \sqrt{2A_{ex}/\mu_0 M_s^2} \tag{3}$$

and takes a value of ~7 nm for Ni. The discretization cell size was set to 4 nm, about half the exchange length, to ensure accurate results. The magnetocrystalline anisotropy (MA) was assumed to be zero for Ni, reflecting the averaging of local MA axes as considered previously.[27,36] The total energy of the system can then be written as

$$\varepsilon = -A_{ex}\boldsymbol{M} \cdot \nabla^2 \boldsymbol{M} - \frac{1}{2}\mu_0 M_s (\boldsymbol{H}_d \cdot \boldsymbol{M}), \tag{4}$$
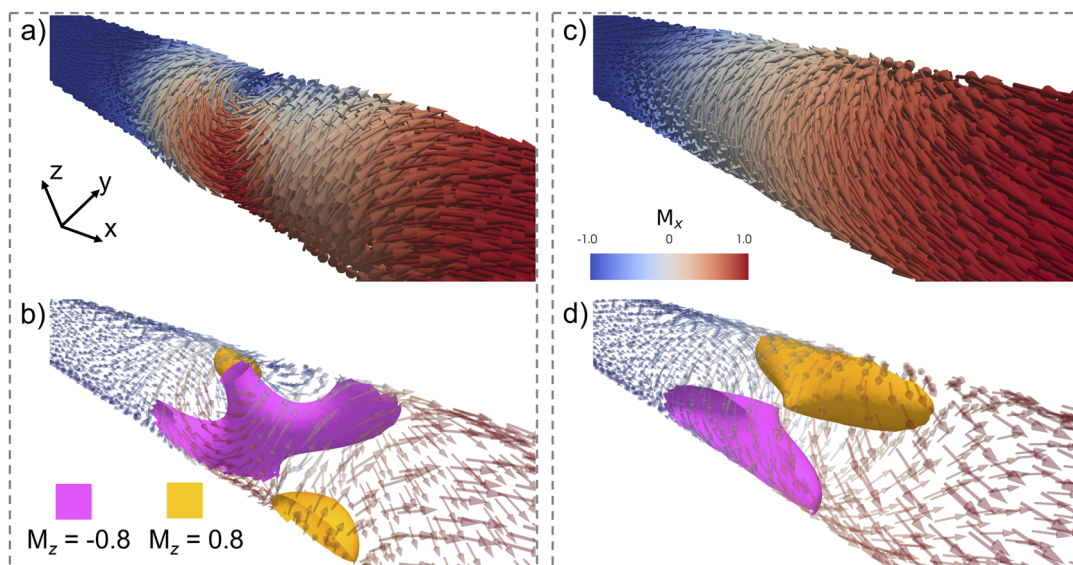

FIG. 1. Simulated magnetization textures of domain walls in a Ni nanowire of 60 nm radius. (a) Surface magnetization texture of an asymmetric transverse wall (ATW). Red and blue hues correspond to positive and negative magnetization M_x along the wire, respectively. (b) Volume isosurfaces of an ATW with magnetization component of $M_z = +0.8$ (orange), and $M_z = -0.8$ (pink). The vortex tube is illustrated by the pink isosurface with the top corresponding to the vortex and the bottom to the anti-vortex. (c) Surface magnetization texture of a Bloch point wall (BPW). (d) Isosurfaces of a BPW. The Bloch point is located between the pink and yellow surfaces. The reader is referred to Figs. S1 and S2 for further visualization of the ATW surface magnetization and volume isosurfaces, respectively.

where $\boldsymbol{H}_d$ is the demagnetizing field.[33] MuMax3 is a graphics processing unit (GPU) accelerated package which is frequently used in the literature for large-scale simulations of cylindrical magnetic NW systems.[14,37] Ubermag is a central processing unit (CPU) based package which uses Python Jupyter Notebooks as a front-end for the Object-Oriented Micromagnetic Framework (OOMMF).[38] For dynamic simulations, the realistic value of $\alpha = 0.1$ was used.[35,39] For relaxation simulations, the damping constant was increased to $\alpha = 1$, to reduce computational time.[31,32]

The simulated NWs have a fixed length of 6 μm such that the aspect ratio of all NWs is greater than 20, rendering the influence of the finite simulation length on the DWs negligible. The radii of the NWs were varied from 50 to 120 nm in steps of 10 nm. Three regions within the wires were then defined, each of 2 μm length. The magnetization in the end regions was fixed, pointing away from the central region, to result in tail-to-tail DWs. In the central region, the initial magnetization was spatially random. The relaxation dynamics was calculated through conjugate gradient energy minimization of the LLG equation in Ubermag[37] and through a Runge–Kutta (RK23) solver in MuMax3.[33] The relaxation was repeated 12 times for each radius, with a different initial random seed for each, to determine the energy densities for each DW type.

Dynamic simulations were performed by unpinning the end regions, and magnetic charges at the extremities of the NW were compensated to emulate an infinitely long wire. Critical fields at which DWs transform into a different state were obtained by incrementing the field applied along the axis of the wire (x-axis) in steps of 0.2 mT. The dynamics of the transformation were then investigated by applying 0.2 mT above the critical field and recording the evolution for 10 ns, sufficient to complete the transformation.

BPWs and ATWs (shown in Fig. 1) are observed as relaxed states for all radii simulated, consistent with previous work.[2,3,5,31,32] Unexpectedly, a new DW type was found for radii above 80 nm. Figure 2(a) illustrates the surface magnetization structure of this new DW for a radius of 90 nm. From an external perspective, it looks similar to an ATW as shown in Fig. 1(a), with a characteristic vortex/anti-vortex pair on opposing surfaces of the nanowire, but with an elongated surface anti-vortex (Fig. S1). The volume isosurfaces, Fig. 2(b), at $M_x = \pm 0.8$, however, reveal a topological difference to the ATW. The isosurfaces show abrupt changes at two points, which are revealed as BPs by the magnetization texture on spherical surfaces of 5 nm radius around these points, as well as the $M_x = 0$, $M_y = 0$, and $M_z = 0$ isosurfaces [Fig. 2(c)]. The local magnetization rotates about the equatorial region of the sphere, which separates the positive and negative components of M_x. The local magnetization tilts toward the poles as the distance from the equator increases, which is consistent with circulating BP spin textures.[40–42] The BP on the left-side rotates counterclockwise (CCW), and the BP on the right-side rotates clockwise (CW). We call this new DW type an asymmetric dual Bloch point wall (ADBPW).

The energies of simulated nanowires with internal DWs as a function of radius are shown in Fig. 3, where the dotted and dashed lines correspond to the magnetostatic and exchange energies respectively, and the solid line corresponds to the total energy. The energies of uniformly magnetized wires with uncompensated magnetic charges at the wire ends are also plotted in
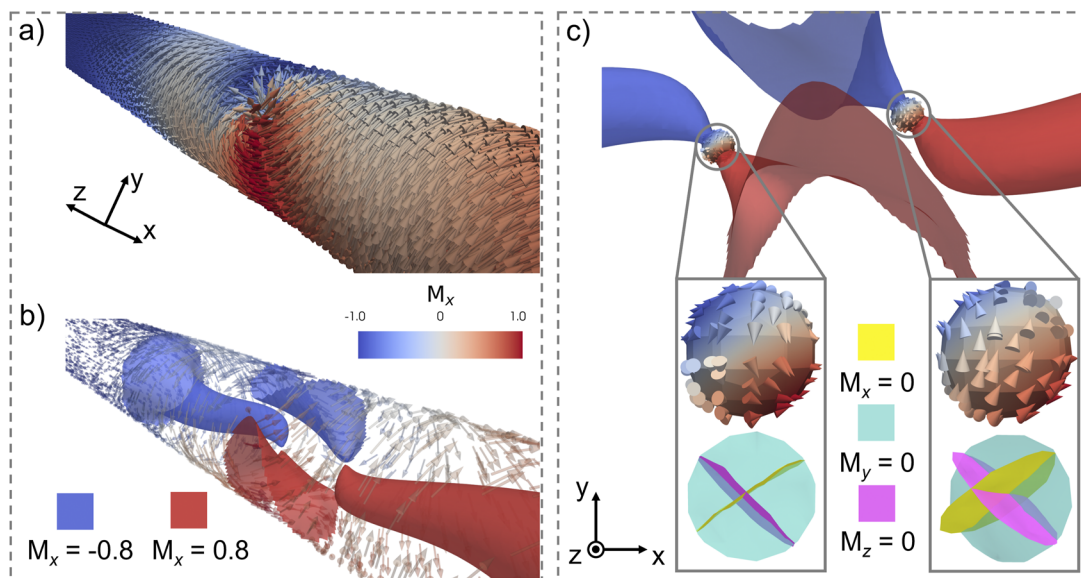

FIG. 2. (a) Surface magnetization texture of the asymmetric dual Bloch point wall (ADBPW) in a wire of 90 nm radius. Red and blue hue correspond to positive and negative magnetization M_x along the wire, respectively. (b) Isosurfaces at which $M_x = +0.8$ (red) and $M_x = -0.8$ (blue). Bloch points (BPs) are found at the intersection of the two isosurfaces. (c) A rotated view of the isosurfaces in (b), with spherical regions plotted at the transition regions. The gray boxes show zoomed in views of the spherical regions with the surface magnetization plotted at the top, and three isosurfaces corresponding to $M_x = 0$, $M_y = 0$, and $M_z = 0$, at the bottom. The intersection of the isosurfaces locates the BPs. The spherical surfaces indicate that the left BP rotates clockwise, and the right BP counterclockwise.
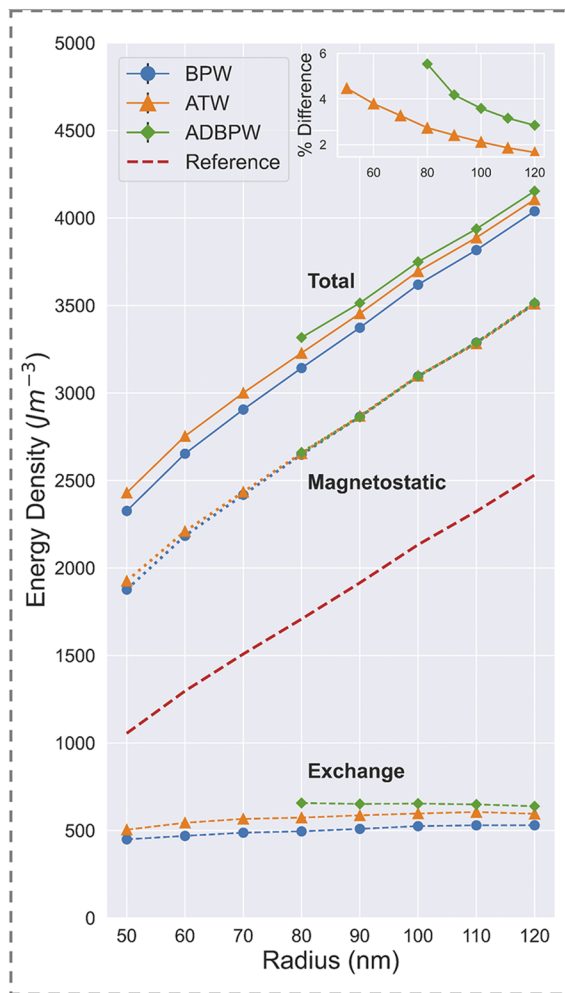
FIG. 3. Nanowire energy density components plotted as a function of radius for all observed DW types. The solid line corresponds to the total, the dotted lines to the magnetostatic and dashed lines to the exchange energy density components. The inset shows the percentage difference in total energy densities between the ground state (BPW), the ATW and ADBPW. The reference line corresponds to a uniformly magnetized wire with uncompensated charges at the wire extremities (and, therefore, a magnetostatic contribution only).

Fig. 3 for reference. All energies are also shown in the supplementary material, Table ST1. Figure 3 illustrates the energy density such that one can adequately compare relative energies across wires of different volumes. We find that across all simulated radii, the BPW is the ground state, which agrees well with the literature.[31,32] The ATW is a metastable excited state with a <5% larger energy compared to the BPW across all simulated radii (see Fig. 3, inset). The ADBPW is instead observed only at radii of 80 nm and higher with 5.53% larger energy than the BPW at $r = 80$ nm and 2.84% larger energy at $r = 120$ nm.

Figures S2 and S3 illustrate, in more detail, the key differences between a conventional ATW and the ADBPW by plotting surfaces of constant magnetization component. In the ATW, Fig. S2, the surface vortex structure with a tube of magnetization with a strong

negative M_z component and a circulating magnetization in M_y penetrates the volume of the wire, providing a means to decrease the magnetostatic energy. As the diameter of the wall increases, it is expected that there will only be a small increase in the exchange energy, mostly dictated by interactions between the extended vortex tube and local magnetization. However, the magnetostatic energy will increase more rapidly, as a greater proportion of the local magnetization within the vortex texture has unfavorable interactions, with both the tube and the tangential magnetization on the nanowire surface. One means to locally reduce such unfavorable magnetostatic interactions is to produce circulating textures within the cross-sectional plane of the wire as seen in the ADBPW, Fig. S3. This produces a stable 3D magnetization texture consisting of a vortex (winding number, $n = +1$) and an anti-vortex ($n = -1$) upon opposing surfaces and two Bloch points of opposing circulation within the volume, overall producing an efficient flux closure. The circulating textures within the cross section have central regions that join the uniformly magnetized regions with high M_x components from both sides, yielding local constraints suitable for BP formation. The symmetry of the magnetization texture yields two BPs on either side of the vortex tube.

The energy densities calculated in Ubermag/OOMMF and MuMax3 are compared for all DW types and across all radii in Fig. S4. All energy density components for the ATWs [Fig. S4(a)] lie within ±0.8%; BPWs [Fig. S4(b)] lie within ±2.5%; and ADBPWs [Fig. S4(c)] lie within ±3.5%. We further validate the energy densities for the three DW types observed where the cell size is varied over the range of 10, 5, and 2.5 nm. Energy density differences are calculated with reference to a cell size of 4 nm. These are shown in Figs. S5 and S6 for ATWs and BPWs, respectively, both simulated at $r = 50$ nm and Fig. S7 for ADBPWs simulated at $r = 80$ nm. All components of energy density differences are less than 10%, and therefore, the choice of a 4 nm discretization is sufficient.

To investigate the stability of the ADBPW against the application of magnetic fields, we have performed simulations with external fields applied along the NW axis, in the positive x-direction, and incremented in steps of 0.2 mT from 0 to 2 mT, where the initial state is the ADBPW at $r = 90$ nm shown in Fig. 2. The magnetization relaxation after each step is simulated, and it was observed that the ADBPW converts to a BPW at a field of 1.6 mT. To determine the dynamics of this transformation from the original relaxed DW state, a static field of 1.6 mT is applied along the long axis in the positive direction and the system is allowed to evolve for 10 ns, saving the magnetization and energies every 100 ps. Figure 4(a) shows the evolution of energy densities between 0 and 3 ns (excluding the Zeeman term). The total energy density difference between the ADBPW and the BPW is 200 J m^{-3} or 5.7% difference, close to the difference observed in Fig. 3 for $r = 90$ nm, which yielded 141 J m^{-3} or 4% difference.

Figures 4(b)–4(g) show snapshots of the surface magnetization (top panels) and the volume isosurfaces (bottom panels) where $M_x = \pm 0.8$. The snapshots are indicated by vertical dashed lines on the energy density evolution in Fig. 4(a). At 0.5 ns [Fig. 4(b)], the structure of the wall has largely remained unchanged (see Fig. 2). The energy density components are all also largely unchanged between 0 and 1.5 ns. Around 1.5 ns [Fig. 4(c)], the energy density components begin to change; the exchange energy decreases and the magnetostatic energy increases such that the total value remains the
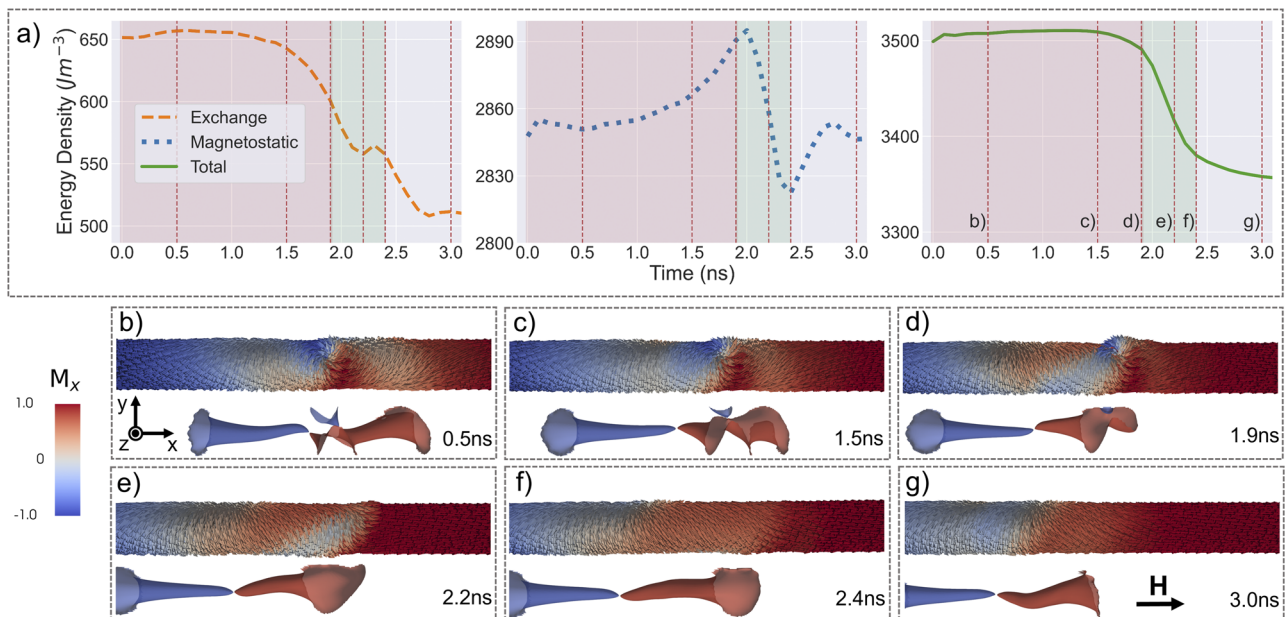
FIG. 4. Conversion of an asymmetric dual Bloch point wall (ADBPW) to a Bloch point wall (BPW) after application of a 1.6 mT external field along the 90 nm radius NW (a) Energy density components as a function of time. The dashed (dotted) lines correspond to the exchange (magnetostatic) energy, and the solid line indicates the total energy (excluding Zeeman). The vertical lines correspond to the snapshots shown in (b)–(g) (b)–(d) 0.5, 1.5, and 1.9 ns – the anti-vortex of the ADBPW moves around the surface of the NW toward the vortex. The isosurfaces, where $M_x = \pm 0.8$, indicate that the right-hand side BP moves toward the vortex, simultaneous to the anti-vortex displacement. This BP-anti-vortex displacement is indicated in (a) by the red region (d)–(f) 1.9, 2.2, and 2.4 ns, the BP is ejected at the surface and the surface magnetization re-aligns after the annihilation of the vortex and anti-vortex. This is indicated by the green region in (a). (g) 3.0 ns - the BP has moved as the NW is magnetized along the external field.

same. The change arises because the anti-vortex moves circumferentially and the BP within the positive M_x region (red, RHS) moves radially toward the vortex. At 1.9 ns [Fig. 4(d)], the magnetostatic energy is almost at its peak value, indicating that the BP within the positive magnetized region is close to the surface (shown by the decreasing size of the blue isosurface). The total energy density decreases rapidly from 1.9 to 2.4 ns. From 2 ns, the BP is no longer visible within the isosurface plots, suggesting that it has been ejected, giving rise to the peak in the magnetostatic energy due to uncompensated magnetic charges at the surface. At 2.2 ns [Fig. 4(e)], the vortex and anti-vortex have annihilated, and the isosurfaces indicate only a single BP within the volume, which is moving in the opposite sense to the applied field along the negative x-direction, along with the entire wall structure. We note that in experiments, the movement of BPWs usually occurs at larger fields (~30 mT, for a Permalloy NW of radius 25 nm and length 2 μm), due to the intrinsic pinning of the BP.[43] Here, the transition provides sufficient dynamics for the BP and wall structure to move some 500 nm along the NW within the 3 ns shown in Fig. 4. This time point also corresponds to a local minimum in the exchange energy density evolution, which is followed by a small rise, which can be attributed to the rotation and re-alignment of the magnetization local to the vortex–anti-vortex annihilation position. In addition, the magnetostatic energy has decreased due to the closure of the vortex tube within the volume. At 2.4 ns [Fig. 4(f)], the local magnetization has realigned through a circumferential wrapping around the NW

surface. This is shown by a sharp increase in the magnetostatic energy where unfavorable alignment of the local magnetization is required to rotate the wrapping around the surface in the same direction. At 3 ns [Fig. 4(g)], the surface magnetization is that of the typical BPW circumferential wrapping, the isosurfaces have continued along the negative x-direction, and all energy components have flattened. From 3 to 10 ns, the energy density components continue to decrease toward the energy density values found in Fig. 3 for a BPW at $r = 90$ nm. We note that the dynamical mechanism observed here is reminiscent of the recently reported domain wall transformations between ATWs and BPWs in cylindrical nanowires of 140 nm diameter.[5] Here, it was observed experimentally and from simulations that an ATW, upon some threshold field, would transform into a BPW via the annihilation of the vortex–anti-vortex pair and subsequent nucleation of a BP at one surface. Interestingly, for single BP systems, the reverse process, though seen in experiments, could not be reproduced in simulations.[5] Here, it was noted that for BPWs, the BP remains at the center of the nanowire cross section, with completely symmetric energy landscape essentially eliminating the movement of the BP from the cross section center. In the ADBPWs realized in this study, the initial off-axis BP positions, in the presence of an external field, provides a route for the BP to reach the surface, promoting the transition. We anticipate that our study will spark further experimental investigations into domain wall topology and associated dynamic transformations in cylindrical magnetic nanowires.

In conclusion, this work has investigated DWs in soft magnetic cylindrical NWs in the radius range of 50–120 nm. The widely reported BPW and ATW are the lowest energy and the first excited state observed, respectively. Importantly, a new metastable DW type, the ADBPW, was found and its magnetization texture is seen to harbor features of both the BPW and the ATW, with two internal BPs adjacent to a vortex tube connecting the surface vortex and antivortex. The stability and dynamics of the ADBPW state were probed under externally applied fields. The ADBPW is found to transform into a BPW via ejection of a BP and relaxation of surface magnetization textures. This work sheds new light on the relationship between different topological spin textures, stabilization of Bloch points, and dynamic transformations between domain walls in cylindrical magnetic nanowires.

See the supplementary material for additional figures comparing typical and the presently studied domain walls, energy density difference studies, and the supplementary material video showing full dynamics of ADBPW to the BPW transformation.

AUTHOR DECLARATIONS

Conflict of Interest

The authors have no conflicts to disclose.

Author Contributions

J. Askey: Data curation (lead); Formal analysis (lead); Writing – original draft (lead); Writing – review & editing (equal). **M. Hunt:** Investigation (equal); Writing – review & editing (equal). **W. Langbein:** Funding acquisition (equal); Project administration (equal); Supervision (equal); Writing – review & editing (equal). **S. Ladak:** Conceptualization (lead); Funding acquisition (equal); Supervision (lead); Writing – original draft (equal); Writing – review & editing (equal).

DATA AVAILABILITY

The data that support the findings of this study are openly available in the Cardiff University data repository and can be accessed at http://doi.org/10.17035/d.2022.0199269274.

REFERENCES

[1] D. Makarov, O. M. Volkov, A. Kákay, O. V. Pylypovskyi, B. Budinská, and O. V. Dobrovolskiy, Adv. Mater. **34**, 2101758 (2022).

[2] S. Da Col, S. Jamet, N. Rougemaille, A. Locatelli, T. O. Mentes, B. S. Burgos, R. Afid, M. Darques, L. Cagnon, J. C. Toussaint, and O. Fruchart, Phys. Rev. B **89**, 180405 (2014).

[3] S. Da Col, S. Jamet, M. Staňo, B. Trapp, S. Le Denmat, L. Cagnon, J. C. Toussaint, and O. Fruchart, Appl. Phys. Lett. **109**, 062406 (2016).

[4] M. Schobitz, A. De Riz, S. Martin, S. Bochmann, C. Thirion, J. Vogel, M. Foerster, L. Aballe, T. O. Mentes, A. Locatelli, F. Genuzio, S. Le-Denmat, L. Cagnon, J. C. Toussaint, D. Gusakova, J. Bachmann, and O. Fruchart, Phys. Rev. Lett. **123**(21), 217201 (2019).

[5] A. Wartelle, B. Trapp, M. Stano, C. Thirion, S. Bochmann, J. Bachmann, M. Foerster, L. Aballe, T. O. Mentes, A. Locatelli, A. Sala, L. Cagnon, J. C. Toussaint, and O. Fruchart, Phys. Rev. B **99**, 024433 (2019).

[6] P. Fischer, D. Sanz-Hernández, R. Streubel, and A. Fernández-Pacheco, APL Mater. **8**, 010701 (2020).

[7] A. Fernández-Pacheco, R. Streubel, O. Fruchart, R. Hertel, P. Fischer, and R. P. Cowburn, Nat. Commun. **8**, 15756 (2017).

[8] D. Sanz-Hernández, A. Hierro-Rodriguez, C. Donnelly, J. Pablo-Navarro, A. Sorrentino, E. Pereiro, C. Magén, S. McVitie, J. M. de Teresa, S. Ferrer, P. Fischer, and A. Fernández-Pacheco, ACS Nano **14**(7), 8084 (2020).

[9] R. Streubel, E. Y. Tsymbal, and P. Fischer, J. Appl. Phys. **129**, 210902 (2021).

[10] A. May, M. Hunt, A. Van Den Berg, A. Hejazi, and S. Ladak, Commun. Phys. **2**, 13 (2019).

[11] A. May, M. Saccone, A. van den Berg, J. Askey, M. Hunt, and S. Ladak, Nat. Commun. **12**, 3217 (2021).

[12] D. W. Wong, I. Purnama, G. J. Lim, W. L. Gan, C. Murapaka, and W. S. Lew, J. Appl. Phys. **119**, 153902 (2016).

[13] J. Fernandez-Roldan, D. Chrischon, L. Dornles, O. Chubykalo-Fesenko, M. Vazquez, and C. Bran, Nanomaterials **8**(9), 692 (2018).

[14] J. A. Fernandez-Roldan, Y. P. Ivanov, and O. Chubykalo-Fesenko, in *Magnetic Nano- and Microwires*, 2nd ed., edited by M. Vázquez (Woodhead Publishing, 2020), p. 403.

[15] J. A. Fernandez-Roldan, R. Perez del Real, C. Bran, M. Vazquez, and O. Chubykalo-Fesenko, Nanoscale **10**(13), 5923 (2018).

[16] R. Hertel, J. Phys.: Condens. Matter **28**, 483002 (2016).

[17] S. S. P. Parkin, M. Hayashi, and L. Thomas, Science **320**(5873), 190 (2008).

[18] S. Parkin and S.-H. Yang, Nat. Nanotechnol. **10**(3), 195 (2015).

[19] J. H. Franken, H. J. M. Swagten, and B. Koopmans, Nat. Nanotechnol. **7**(8), 499 (2012).

[20] N. A. Alsharif, F. A. Aleisa, G. Liu, B. S. Ooi, N. Patel, T. Ravasi, J. S. Merzaban, and J. Kosel, ACS Appl. Bio Mater. **3**(8), 4789 (2020).

[21] A. Sharma, Y. Zhu, S. Thor, F. Zhou, B. Stadler, and A. Hubel, IEEE Trans. Magn. **49**(1), 453 (2013).

[22] C. Bran, Y. P. Ivanov, J. Kosel, O. Chubykalo-Fesenko, and M. Vazquez, Nanotechnology **28**, 095709 (2017).

[23] E. Berganza, M. Jaafar, C. Bran, J. A. Fernández-Roldán, O. Chubykalo-Fesenko, M. Vázquez, and A. Asenjo, Sci. Rep. **7**, 11576 (2017).

[24] C. Bran, E. Berganza, J. A. Fernandez-Roldan, E. M. Palmero, J. Meier, E. Calle, M. Jaafar, M. Foerster, L. Aballe, A. Fraile Rodriguez, R. P. del Real, A. Asenjo, O. Chubykalo-Fesenko, and M. Vazquez, ACS Nano **12**, 5932 (2018).

[25] X. Y. Zhang, G. H. Wen, Y. F. Chan, R. K. Zheng, X. X. Zhang, and N. Wang, Appl. Phys. Lett. **83**(16), 3341 (2003).

[26] M. Hunt, M. Taverne, J. Askey, A. May, A. Van Den Berg, Y.-L. D. Ho, J. Rarity, and S. Ladak, Materials **13**(3), 761 (2020).

[27] J. Askey, M. O. Hunt, W. Langbein, and S. Ladak, Nanomaterials **10**(3), 429 (2020).

[28] G. Williams, M. Hunt, B. Boehm, A. May, M. Taverne, D. Ho, S. Giblin, D. Read, J. Rarity, R. Allenspach, and S. Ladak, Nano Res. **11**, 845 (2018).

[29] C. Magén, J. Pablo-Navarro, and J. M. De Teresa, Nanomaterials **11**(2), 402 (2021).

[30] A. Fernández-Pacheco, L. Skoric, J. M. De Teresa, J. Pablo-Navarro, M. Huth, and O. V. Dobrovolskiy, Materials **13**(17), 3774 (2020).

[31] C. A. Ferguson, D. A. Maclaren, and S. McVitie, Magn. Magn. Mater. **381**, 457 (2015).

[32] S. Jamet, N. Rougemaille, J. C. Toussaint, and O. Fruchart, in *Magnetic Nano- and Microwires*, edited by M. Vazquez (Woodhead Publishing, 2015), p. 783.

[33] A. Vansteenkiste, J. Leliaert, M. Dvornik, M. Helsen, F. Garcia-Sanchez, and B. Van Waeyenberge, AIP Adv. **4**, 107133 (2014).

[34]M. Beg, M. Lang, S. Holt, R. A. Pepper, T. Kluyver, J. Mulkers, J. Leliaert, and H. Fangohr (2022). "ubermag: Meta package for Ubermag project," Zenodo. https://doi.org/10.5281/zenodo.3539495.

[35]M. Beg, R. A. Pepper, and H. Fangohr, AIP Adv. **7**, 056025 (2017).

[36]L. C. C. Arzuza, R. López-Ruiz, D. Salazar-Aravena, M. Knobel, F. Béron, and K. R. Pirota, J. Magn. Magn. Mater. **432**, 309 (2017).

[37]S. Ruiz-Gómez, C. Fernández-González, E. Martínez, V. Raposo, A. Sorrentino, M. Foerster, L. Aballe, A. Mascaraque, S. Ferrer, and L. Pérez, Nanoscale **12**(34), 17880 (2020).

[38]M. J. Donahue and D. G. Porter, OOMMF User's Guide, Version 1.0. Interagency Report No. NISTIR 6376, 1999.

[39]R. Hertel, J. Magn. Magn. Mater. **249**(1–2), 251 (2002).

[40]A. Thiaville, J. M. Garcia, R. Dittrich, J. Miltat, and T. Schrefl, Phys. Rev. B **67**(9), 094410 (2003).

[41]S. K. Kim and O. Tchernyshyov, Phys. Rev. B **88**(17), 174402 (2013).

[42]O. V. Pylypovskyi, D. D. Sheka, and Y. Gaididei, Phys. Rev. B **85**(22), 224401 (2012).

[43]H.-G. Piao, J.-H. Shim, D. Djuhana, and D.-H. Kim, Appl. Phys. Lett. **102**, 112405 (2013).